Advanced Fiber Materials (2023) 5:1685–1698
https://doi.org/10.1007/s42765-023-00295-3

RESEARCH ARTICLE

Electrospun $ZnSnO_3$/PVDF-HFP Nanofibrous Triboelectric Films for Efficient Mechanical Energy Harvesting

Venkata Siva Kavarthapu[1] · Sontyana Adonijah Graham[1] · Punnarao Manchi[1] · Mandar Vasant Paranjape[1] · Jae Su Yu[1]

Received: 25 January 2023 / Accepted: 25 April 2023 / Published online: 23 May 2023

Abstract

Nowadays, triboelectric nanogenerators (TENGs) are one of the most emerging technologies owing to their easy and cost-effective device structure. TENGs can harvest mechanical energy from our living environment. Herein, we synthesized dielectric zinc tin oxide ($ZnSnO_3$) nanoparticles (NPs) by a hydrothermal technique. The $ZnSnO_3$ NPs provide a dielectric and piezoelectric effect, which can efficiently enhance the output electrical performance of the proposed TENG. The prepared $ZnSnO_3$ NPs were embedded into a polyvinylidene fluoride hexafluoropropylene (PVDF-HFP) polymer to prepare $ZnSnO_3$/PVDF-HFP nanofibrous films to fabricate a TENG. The output performance of TENG was investigated and optimized by varying the loading concentration of $ZnSnO_3$ NPs in PVDF-HFP fibrous films. The highest voltage, current, charge density, and power density from the fabricated TENG were achieved as ~ 138 V, ~ 5 μA, ~ 52 μC/m^2, and ~ 1.6 W/m^2, respectively. Additionally, the robustness of the TENG was studied via the long-term mechanical stability test. Finally, the practical and real-time application of the TENG was demonstrated by harvesting mechanical energy to power low-power portable electronic devices. Furthermore, the materials used in the TENG were combined into a skipping rope to harvest biomechanical/mechanical energy while exercising.

Keywords $ZnSnO_3$ nanoparticles · $ZnSnO_3$/PVDF-HFP fibrous films · Triboelectric nanogenerators · Mechanical energy harvesting

Introduction

Energy plays a crucial role in the day-to-day lives of humans, and it is mostly extracted from conventional fossil fuels. Due to the huge energy demand, the limited amount of fossil fuels, and their adverse effects on the environment/human life, it is essential to find alternative sustainable energy sources [1–3]. Mechanical energy is one of the renewable green energy sources, which is abundantly available in surrounding nature and can be converted into electricity using various technologies like piezoelectric, triboelectric, and electromagnetic nanogenerators [4, 5]. Triboelectric nanogenerators (TENGs) have gained a lot of interest due to their superiority to convert any type of mechanical energy into electricity based on the combined effects of triboelectrification and electrostatic induction [6]. Moreover, TENG possesses numerous advantages including cost-effectiveness, simple device architecture, easy fabrication process, high output power, safety, etc. [7–9]. The electronic gadgets used in day-to-day life consume more electricity than that produced by TENG. Therefore, many efforts were taken to improve the electrical output of the TENG through various strategies like improvement in the dielectric property of triboelectric material, surface engineering, hybrid device structure, etc. Fabrication of composite films that utilize a combined synergistic effect (piezoelectric/triboelectric) is one of the efficient ways to enhance the electrical output from resultant energy harvesting systems [10, 11]. The surface area as well as the surface charge density of the triboelectric film is crucial parameter directly proportional to the electrical output from the TENG [12, 13]. Electrospinning which is one of the most prominent thin film fabrication techniques has been used in many fields including energy storage,

✉ Jae Su Yu
jsyu@khu.ac.kr

[1] Department of Electronics and Information Convergence Engineering, Institute for Wearable Convergence Electronics, Kyung Hee University, 1732 Deogyeong-daero, Giheung-gu, Yongin-Si, Gyeonggi-do 17104, Republic of Korea

sensing, textiles, filtration, etc. [11, 12, 14, 15]. The advantageous characteristics of electrospinning nanofibrous films, such as large specific surface area, inherent roughness, hierarchical porous structure, homogeneously distributed fibrous network, etc., can significantly increase their surface charge density. Moreover, the diameter of the nanofibers can also be easily altered by varying the applied electric field and flow rate [16, 17]. This further enhances the overall electrical performance and wearability of the corresponding TENGs. In the electrospinning technique, a high electric field is usually employed to create nanofibers from the viscous liquid material. In the case of ferroelectric materials (e.g., polyvinylidene fluoride hexafluoropropylene (PVDF-HFP)), the applied high electric field during the electrospinning technique polarizes its dipole and hence removes the necessity of the polling process to obtain an efficient electrical output from the corresponding TENG [18]. Lin et al. fabricated reduced graphene oxide-PVDF composite fibrous film and utilized it for the fabrication of high-performance TENG. They observed that the TENG with fibrous film produces enhanced electrical output as compared to conventionally fabricated composite film-based TENG [20]. Similar results were reported by Byeong et al. for electrospun ion gel-based mechanical energy harvesters [21].

On the other hand, PVDF-HFP is a well-known piezoelectric polymer with outstanding stability and high flexibility that can be utilized as a negative triboelectric film for TENG fabrication [22]. PVDF-HFP has three phases, i.e., α, β, and γ. Among them, β phase exhibits the highest piezoelectric coefficient, which makes it a suitable material for TENG fabrication. $ZnSnO_3$ is a well-known inorganic lead-free metal oxide material that possesses advantageous physical properties like high dielectric constant, piezoelectricity, electrical conductivity, etc. The $ZnSnO_3$ exhibits strong piezoelectric properties and large spontaneous polarization [23]. The presence of large polarization is due to the large displacement of the zinc (Zn) based on a strong covalent bond between three oxygen (O) and Zn atoms and is significantly larger than other oxides like ZnO, $BaTiO_3$, $KNbO_3$, etc. [24]. Therefore, combining it with PVDF-HFP could result in a composite film with a very high piezoelectricity coefficient [25].

In this work, we proposed a $ZnSnO_3$/PVDF-HFP nanofibrous film-based TENG for efficient mechanical energy harvesting. Initially, $ZnSnO_3$ nanoparticles (NPs) were synthesized and loaded into the PVDF-HFP polymer to form various composite solutions. The prepared composite solutions were further electrospun to fabricate various $ZnSnO_3$/PVDF-HFP fibrous films. The applied high voltage during the electrospinning process electrically polarizes the fibrous film which removes the necessity of the post-poling process to get the enhanced electrical output from the TENG [26, 27]. Various TENGs were fabricated by utilizing the composite fiber films attached to aluminum (Al) electrode as a negative triboelectric medium which was operated against the positive Al triboelectric film. All the fabricated TENGs were operated under constant external force in contact-separation mode and the produced electrical output was thoroughly investigated to find an optimum concentration of $ZnSnO_3$ inside the composite film. The optimized $ZnSnO_3$/PVDF-HFP composite film-based TENG produces superior electrical output as compared to the other TENGs consisting of PVDF-HFP and $ZnSnO_3$/PVDF-HFP composite fibrous films. The fabricated TENG produced highly stable electrical output, showing its reliability in real-life applications to harvest mechanical energy into electricity. The highly efficient electrical output produced by the TENG was further supplied to power a small liquid crystal display (LCD) timer as well as light-emitting diodes (LEDs). Furthermore, biomechanical energy generated from the various human movements was successfully harvested utilizing the optimized TENG device. A number of similar TENGs were fabricated to check the reproducibility of the proposed device and further integrated inside the skipping rope to mechanical movements generated while skipping into electricity. The proposed TENG can be utilized as a reliable mechanical energy harvesting device over a large scale to fulfill the requirement of electricity in daily life.

Experimental Section

Materials

Zinc acetate dihydrate ($Zn(CH_3COO)_2{\cdot}2H_2O$), tin chloride pentahydrate ($SnCl_4{\cdot}5H_2O$), sodium hydroxide (NaOH), and PVDF-HFP pellets with a purity of ≥ 98% were purchased from Sigma-Aldrich Co. Ltd., South Korea. Dimethyl sulfoxide (DMSO) with a purity of 99.8% and Al adhesive tape were purchased from Junsei Chemical Co., Ltd., Japan and Ducksung Hightech Co., Ltd., South Korea, respectively. Acetone (C_3H_6O) and ethanol (C_2H_5OH) with a purity of 99.8% were purchased from ChemiTop Co. Ltd., South Korea. All the chemicals and reagents were used directly without any purification.

Synthesis Process of $ZnSnO_3$ NPs

Figure 1 shows the synthesis procedure of the $ZnSnO_3$ NPs via a hydrothermal chemical method and the fabrication of the TENG. Figure 1a shows the preparation of precursor solutions A and B. Solution A was prepared by mixing 0.05 molar (M) of NaOH and 0.05 M of $SnCl_4{\cdot}5H_2O$ into 45 mL de-ionized (DI) water, and solution B was prepared by adding 0.05 M $Zn(CH_3COO)_2{\cdot}2H_2O$ to 45 mL DI water. Solution A and solution B were mixed vigorously under constant magnetic stirring at 400 rotations per minute (rpm) for 30

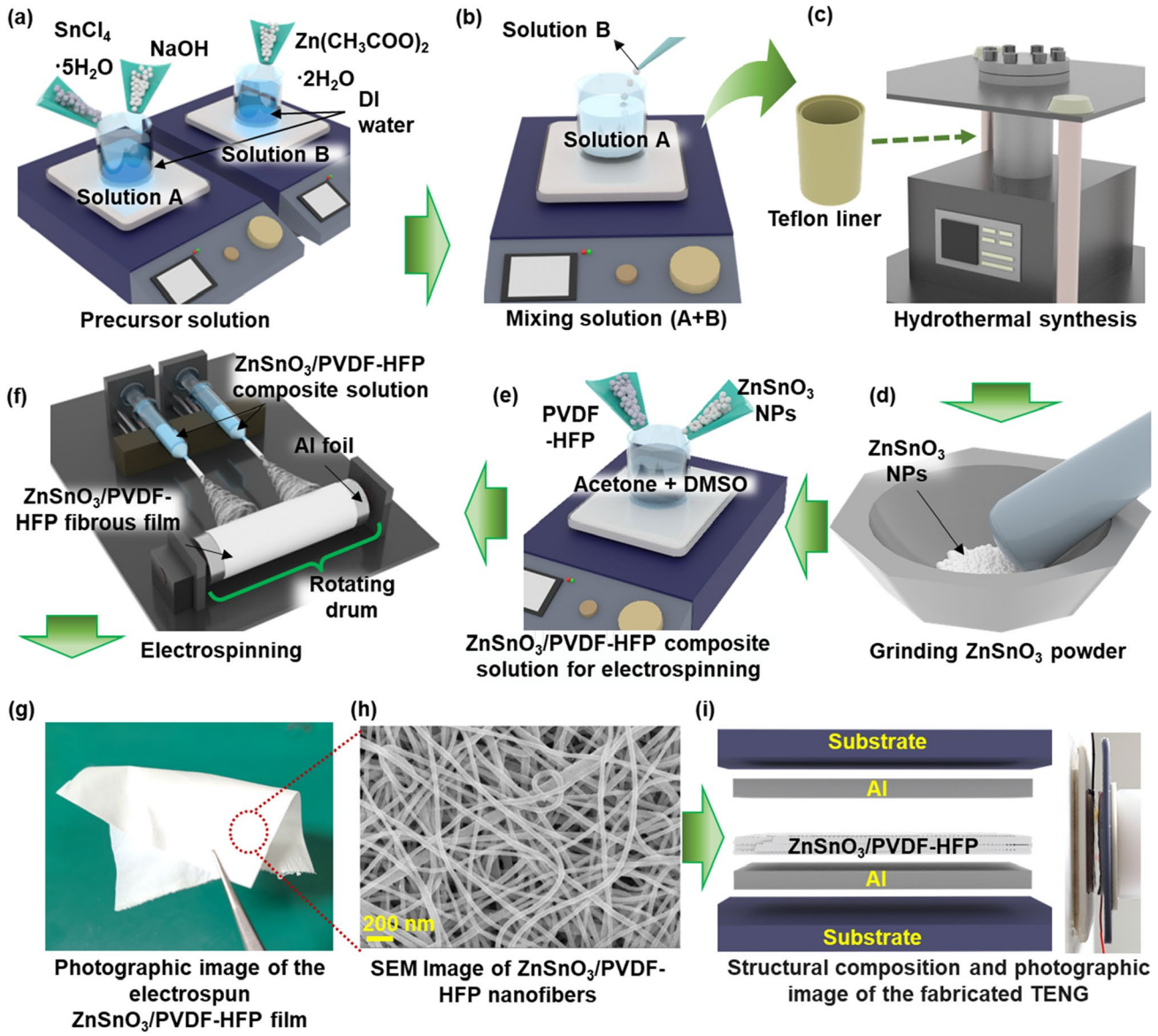

Fig. 1 Schematic representation and fabrication process of the $ZnSnO_3$/PVDF-HFP fibrous film-based TENG. **a–d** Synthesis process of the $ZnSnO_3$ NPs by a hydrothermal method. **e, f** Preparation process of $ZnSnO_3$/PVDF-HFP precursor solution and electrospinning process of solution on the Al foil. **g** Photographic image and **h** magnified FE-SEM image of the electrospun $ZnSnO_3$/PVDF-HFP fibrous film. **i** Components and photographic image of the fabricated TENG

min. Thereafter, as shown in Fig. 1b, solution B was added dropwise to solution A and magnetically stirred at 400 rpm for 1 h. The well-dissolved precursor solution was transferred to a 120 mL Teflon liner which was further kept inside the autoclave and temperature was maintained at 150 °C for 10 h as shown in Fig. 1c. After completing the hydrothermal process, the autoclave was allowed to cool down to room temperature, and the obtained precipitate was washed several times with DI water and ethanol for the removal of residual impurities. The obtained $ZnSnO_3$ precipitate was dried in a hot air oven at 100 °C for 12 h. Finally, as shown in Fig. 1d, the synthesized powder was ground smoothly and used for further characterization.

Preparation Process of $ZnSnO_3$/PVDF-HFP Fibrous Films

To prepare the $ZnSnO_3$/PVDF-HFP fibrous films, initially, 10 mL of DMSO and 10 mL of acetone were mixed. Afterward, as shown in Fig. 1e, 10 wt% of PVDF-HFP pallets were added to the DMSO/acetone solution and magnetically stirred (300 rpm) for 30 min at 100 °C. The synthesized $ZnSnO_3$ NPs with various concentrations (i.e., 0, 1, 2, 3, 4,

and 5 wt%) were loaded into the prepared PVDF-HFP solution and magnetically stirred for 30 min at 100 °C to form a homogeneous composite solution. Figure 1f shows the electrospinning process where the prepared $ZnSnO_3$/PVDF-HFP polymer solution was electrospun on an Al foil. Initially, the prepared $ZnSnO_3$/PVDF-HFP composite solution was carefully transferred into a glass syringe consisting of a metallic 23-gauge needle. Besides, the Al foil was wrapped around the electrospinning rotational drum which is electrically negative. The electrospinning voltage was maintained at 10 kV to form the fibrous films. The distance between the collector and the syringe needle was maintained at 15 cm. The solution flow rate during the electrospinning was maintained at 1 mL/h. Afterward, a thin fibrous film was obtained on the Al foil which was dried in an oven at 40 °C for 1 h. The $ZnSnO_3$/PVDF-HFP fibrous film was peeled off from the Al foil and cut into the desired dimensions for further experimental use. The photographic image and field-emission scanning electron microscope (FE-SEM) image of the prepared $ZnSnO_3$/PVDF-HFP fibrous film are shown in Fig. 1g, h, respectively. The bare PVDF-HFP fibrous film was also prepared in the same procedure as the composite film without adding the $ZnSnO_3$ NPs.

Fabrication Process of TENG Device

The TENG structure and its components are shown in Fig. 1i. Initially, the prepared $ZnSnO_3$/PVDF-HFP fibrous films were cut with a 2 × 2 cm^2 dimension and attached to the Al electrode (2 × 2 cm^2), which was operated as a negative triboelectric film. Besides, the same dimension of another Al electrode was used as a positive triboelectric film as well as an electrode. The two triboelectric films were attached to 3D-printed plastic acrylonitrile butadiene styrene (ABS) supporting substrates with the dimension of 4 × 4 cm^2. The photographic image of the fabricated TENG device is shown in Fig. 1i.

Results and Discussion

Figure 2 shows the material characterization of the prepared $ZnSnO_3$ NPs and the bare PVDF-HFP and $ZnSnO_3$/PVDF-HFP composite films. Figure 2a and b shows the FE-SEM image of the synthesized $ZnSnO_3$ NPs and the 3 wt% $ZnSnO_3$/PVDF-HFP fibrous film. To ensure the homogeneity in the synthesized $ZnSnO_3$, energy dispersive X-ray (EDX) spectroscopy was employed as shown in Fig. S1a–c of the Supporting Information (SI). The EDX mapping images of Zn, tin (Sn), and O subelements in $ZnSnO_3$ NPs are shown in Fig. S1d–f of the SI. It is clear that the subelements of $ZnSnO_3$ are uniformly distributed over an acquired region. The surface topography of the fabricated PVDF-HFP and various $ZnSnO_3$/PVDF-HFP fibrous films was analyzed by the FE-SEM images as shown in Fig. S2a–f of the SI. It was observed that all the fabricated PVDF-HFP-based fibrous films had a homogeneous and uniform distribution of fibers with the same diameter. Furthermore, to confirm the $ZnSnO_3$ loading in PVDF-HFP fibrous films, the top-view FE-SEM image of 3 wt% $ZnSnO_3$/PVDF-HFP fibrous film was obtained at high magnification as shown in Fig. 2b. Fig. S3a of the SI shows the uniform distribution of all the subelements including carbon (C), fluorine (F), Zn, Sn, and O in the prepared 3 wt% $ZnSnO_3$/PVDF-HFP fibrous film. The EDX spectrum analysis confirmed the Zn, Sn, O, C, and F elements in the synthesized $ZnSnO_3$/PVDF-HFP fibrous film, as shown in Fig. S3b of the SI. Figure 2c shows the XRD patterns of the $ZnSnO_3$ NPs and the PVDF-HFP and 3 wt% $ZnSnO_3$/PVDF-HFP fibrous films and their comparison with standard reference XRD data (ICDD-00-028-1486). The diffraction peaks of $ZnSnO_3$ NPs were observed to be 24.973°, 33.203°, 37.768°, 51.134°, and 64.678° [28–30]. The XRD pattern of $ZnSnO_3$/PVDF-HFP nanofibers exhibited both PVDF-HFP and $ZnSnO_3$ peaks, which implies the coexistence of PVDF-HFP and $ZnSnO_3$ NPs in the fabricated composite nanofibers. These results also suggest that the perovskite structure of $ZnSnO_3$ NPs remained undisturbed during the electrospinning process. To find the chemical oxidation states and elemental composition of the synthesized $ZnSnO_3$ NPs, X-ray photoelectron spectroscopy (XPS) analysis was performed as shown in Fig. S4 of the SI and Fig. 2d–f. The obtained XPS spectra were calibrated according to the characteristic peak of C at the binding energy of 284.8 eV. The complete scan spectrum of the $ZnSnO_3$ in Fig. S4 of the SI shows the presence of Zn 2p, Sn 3d, and O 1s subelements. Furthermore, Fig. 2d shows the Zn 2p core-level spectrum consisting of two separate peaks of Zn $2p_{1/2}$ and Zn $2p_{3/2}$ at 1043.98 and 1020.88 eV, respectively [31]. As shown in Fig. 2e, the Sn 3d core-level spectrum revealed intense binding energy peaks at the binding energies of 493.98 and 485.58 eV for Sn $3d_{3/2}$ and Sn $3d_{5/2}$ valance states, respectively with a splitting energy of 8.4 eV [32]. Figure 2f shows the core-level XPS spectrum of O 1s. The peaks located at 529.48 and 530.78 eV are attributed to the lattice oxygen (O_L) and available oxygen vacancies (O_V), respectively [33]. It is well-known that the $ZnSnO_3$ has a relatively high dielectric constant at room temperature. To verify this, the frequency-dependent dielectric constant of the synthesized $ZnSnO_3$ NPs was measured as shown in Fig. S5a of the SI. As observed, the synthesized $ZnSnO_3$ NPs exhibited a high dielectric constant value of ~ 2,338.37 at a low frequency of 100 Hz, which decreased to ~ 8.056 at a higher frequency and was further stable. Besides, Fig. S5b of the SI shows the measured dielectric loss of the synthesized $ZnSnO_3$ NPs. The dielectric loss measurement also displays a similar trend with high dielectric loss at a low

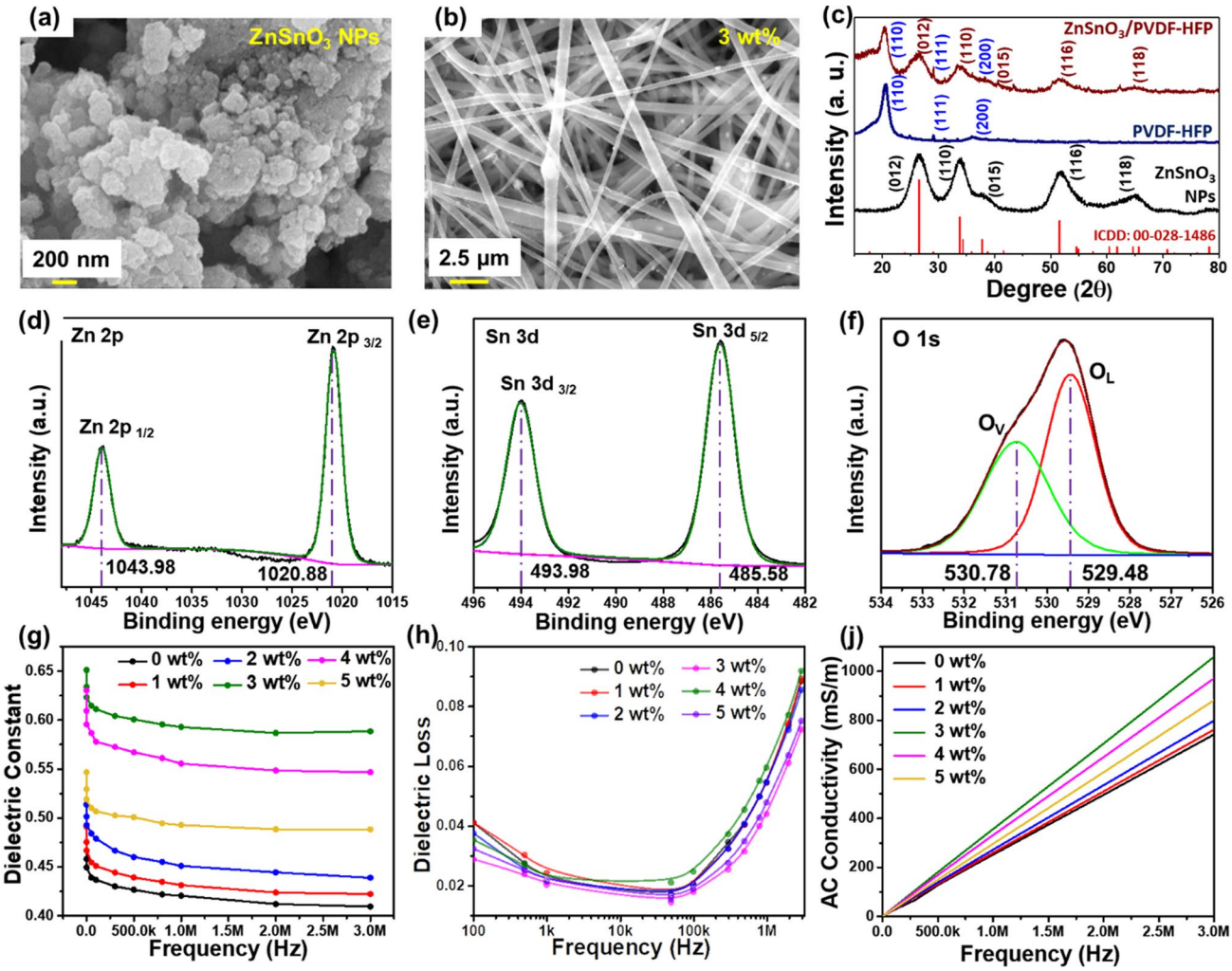

Fig. 2 **a, b** FE-SEM images of $ZnSnO_3$ NPs and $ZnSnO_3$/PVDF-HFP fibrous films. **c** XRD patterns of the prepared $ZnSnO_3$ NPs, PVDF-HFP, and $ZnSnO_3$/PVDF-HFP. XPS spectra of **d** Zn 2p, **e** Sn 3d, and **f** O 1s. **g–i** Dielectric constant, dielectric loss, and AC conductivity values of the $ZnSnO_3$/PVDF-HFP fibrous films with different $ZnSnO_3$ concentrations (i.e., 0, 1, 2, 3, 4, and 5 wt%)

frequency of 100 Hz and it gradually decreases with increasing the frequency range up to 8 MHz. Fig. S5c of the SI shows the measured alternating current (AC) conductivity of the synthesized $ZnSnO_3$ NPs. It was observed that the AC conductivity of the pallet increased while increasing the applied frequency and reached the maximum value of 21.2 S/m at 8 MHz.

The electrical output from any TENG is highly dependent on the dielectric properties of the utilized triboelectric film in it. As the dielectric constant of the triboelectric film increases, the electrical performance of the TENG should also increase [42]. Mixing high dielectric constant $ZnSnO_3$ NPs as a filler material inside the PVDF-HFP could enhance the electrical output from the respective TENG as well as its dielectric constant. Therefore, the dielectric properties and the AC conductivity of the various $ZnSnO_3$/PVDF-HFP fibrous films were studied systematically under different frequencies ranging from 100 Hz to 3 MHz, as shown in Fig. 2g–i. The frequency-dependent dielectric constant values of the $ZnSnO_3$/PVDF-HFP fibrous films with various filler concentrations (i.e., 0, 1, 2, 3, 4, and 5 wt%) are shown in Fig. 2g. The dielectric constant was reduced with increasing the frequency, which is due to the characteristics of interfacial polarization. The dielectric constant of the prepared $ZnSnO_3$/PVDF-HFP fibrous films was enhanced by increasing the filler amount up to 3 wt%, and the highest value of ~0.651 at 100 Hz was archived. With further increasing the filler amount up to 5 wt%, the dielectric constant value decreased to ~0.547. This might be due to the aggregation of the filler at higher concentrations [34]. Figure 2h shows the dielectric loss values of the various $ZnSnO_3$/PVDF-HFP fibrous films measured at room temperature in the frequency range from 100 Hz to 3 MHz. Similarly, the AC conductivity

for all the $ZnSnO_3$/PVDF-HFP fibrous films with various $ZnSnO_3$ concentrations was measured as shown in Fig. 2i. Similar to the dielectric constant, the AC conductivity of the PVDF-HFP fibrous films was increased with increasing the $ZnSnO_3$ concentration up to 3 wt%. This can be attributed to the enhanced interface conductivity between the $ZnSnO_3$ NPs and PVDF-HFP polymer matrix [35]. Further increase in concentration (> 3 wt%) of $ZnSnO_3$ in PVDF-HFP results in reducing the dielectric constant of the fibrous film. Increased concentration of $ZnSnO_3$ filler inside the PVDF-HFP matrix causes an agglomeration of them with nonhomogeneous nature. This could be one of the reasons behind the decreased AC conductivity in fibrous films with higher $ZnSnO_3$ concentration [36]. The dielectric loss gradually decreased with increasing the filler concentration, which is related to the interfacial polarization between the $ZnSnO_3$ NPs and PVDF-HFP polymer. All the prepared $ZnSnO_3$/PVDF-HFP fibrous films exhibited a low dielectric loss by increasing the applied frequency [37].

The β phase of the PVDF is also the most favorable parameter to get an enhanced electrical output from the respective TENG. As discussed earlier, the synthesized $ZnSnO_3$ exhibits a high dielectric constant. Mixing it in a PVDF-HFP polymer matrix could enhance the dielectric constant and β phase of the resultant PVDF-HFP-based fibrous films. As discussed above, the dielectric constant of the PVDF fibrous film increased with the increasing the $ZnSnO_3$ concentration in it. The $ZnSnO_3$/PVDF-HFP with 3 wt% $ZnSnO_3$ concentration exhibited the highest dielectric constant. Therefore, the bare PVDF-HFP and 3 wt% $ZnSnO_3$/PVDF-HFP fibrous films were analyzed through the Fourier transform infrared spectroscopy (FTIR) technique to find out the change in the amount of β phase. The obtained FTIR spectra of the bare PVDF-HFP and 3 wt% $ZnSnO_3$/ PVDF-HFP fibrous films are shown in Fig. S6 of the SI. Thereafter, by utilizing α and β crystal peak intensities and Beer-Lambert's law, the formed β phase fraction (F_β) in the fabricated thin films was calculated. The mathematical equation for the calculation of β phase of the thin films is shown below [38, 39].

$$F_\beta = \frac{A_\beta}{\left(\frac{K_\beta}{K_\alpha}\right)A_\alpha + A_\beta} \times 100\% \quad (1)$$

where A_α and A_β are the absorbed energies at 766 and 840 cm^{-1}, whereas the ratio of absorption coefficient observed at a respective wavelength from the FTIR spectrum is $K_\beta/K_\alpha = 1.262$. The maximum F_β value for PVDF-HFP is ~ 38.54%. Meanwhile, for the 3 wt% $ZnSnO_3$/PVDF-HFP fibrous film, it reaches to 41.15% which is higher than that of the PVDF-HFP film. This is mainly due to the interaction between the PVDF-HFP polymer and $ZnSnO_3$ NPs, which leads to the improvement of F_β.

Figure 3a shows the schematic diagram illustrating the working mechanism of the vertical contact-separation mode TENG. The TENG consists of $ZnSnO_3$/PVDF-HFP/Al employed as the negative triboelectric material (– ve) vs. Al foil as the positive triboelectric material (+ ve). At first, both the triboelectric friction layers are in full contact with each other by an externally applied force, and the corresponding – ve and + ve charges are induced on their surfaces as shown in Fig. 3a–i. When an external force is removed, the $ZnSnO_3$/PVDF-HFP/Al layer starts to separate from the Al electrode as shown in Fig. 3a–ii. The electrons from the bottom Al electrode flow through an external circuit towards the top Al electrode layer. The two triboelectric friction layers completely separate as shown in Fig. 3a–iii. The TENG results in a charge equilibrium state where there is no flow of charges. Once again, when an external force is applied to the TENG, the two triboelectric layers come into contact with each other in Fig. 3a–iv, and the charges flow back through an external circuit, thus leading to an electrostatic equilibrium between both electrodes. Likewise, with the periodically applied external mechanical force on the TENG, the $ZnSnO_3$/PVDF-HFP/Al and Al triboelectric friction layers continuously contact and separate to generate electricity. The electrical potential generated during each complete cycle of the TENG was investigated by a finite elemental simulation tool (COMSOL Multiphysics simulation software), as shown in Fig. 3b. The TENG was designed with an area of 2×2 cm^2, and Al adhesive tape was attached to the $ZnSnO_3$/PVDF-HFP fibrous film with a dielectric constant (ε_r) of 0.65 calculated at 100 Hz and a thickness of 35 μm, which serves as a top triboelectric layer. Besides, Al film with $\varepsilon_r = 9.5$ and a thickness of 60 μm acts as a bottom triboelectric layer. Both the friction layers move at a finite distance. The optimal performance is obtained. However, the $ZnSnO_3$/PVDF-HFP-based TENG shows a higher potential difference compared to the bare PVDF-HFP-based TENG. From the simulation result, the minimal potential is generated across the TENG during the full contact and separated states. Meanwhile, the maximum potential is generated during the separation and approaching states. This confirms the generated electric potential across the two triboelectric friction layers.

The generated electrical voltage, current, and charge density curves of the TENGs based on the PVDF-HFP fibrous films with various $ZnSnO_3$ NPs concentrations (i.e., 0, 1, 2, 3, 4, and 5 wt%) were measured, as shown in Fig. 3c–e. By adding the filler material in the PVDF-HFP polymer up to 3 wt%, the output performance of the TENG was enhanced from ~ 35 V, ~ 1 μA, 15 μC/m^2 to ~ 138 V, ~ 5 μA, 52 μC/m^2, respectively. This enhancement in the electrical performance is mainly achieved due to the enhanced dielectric constant

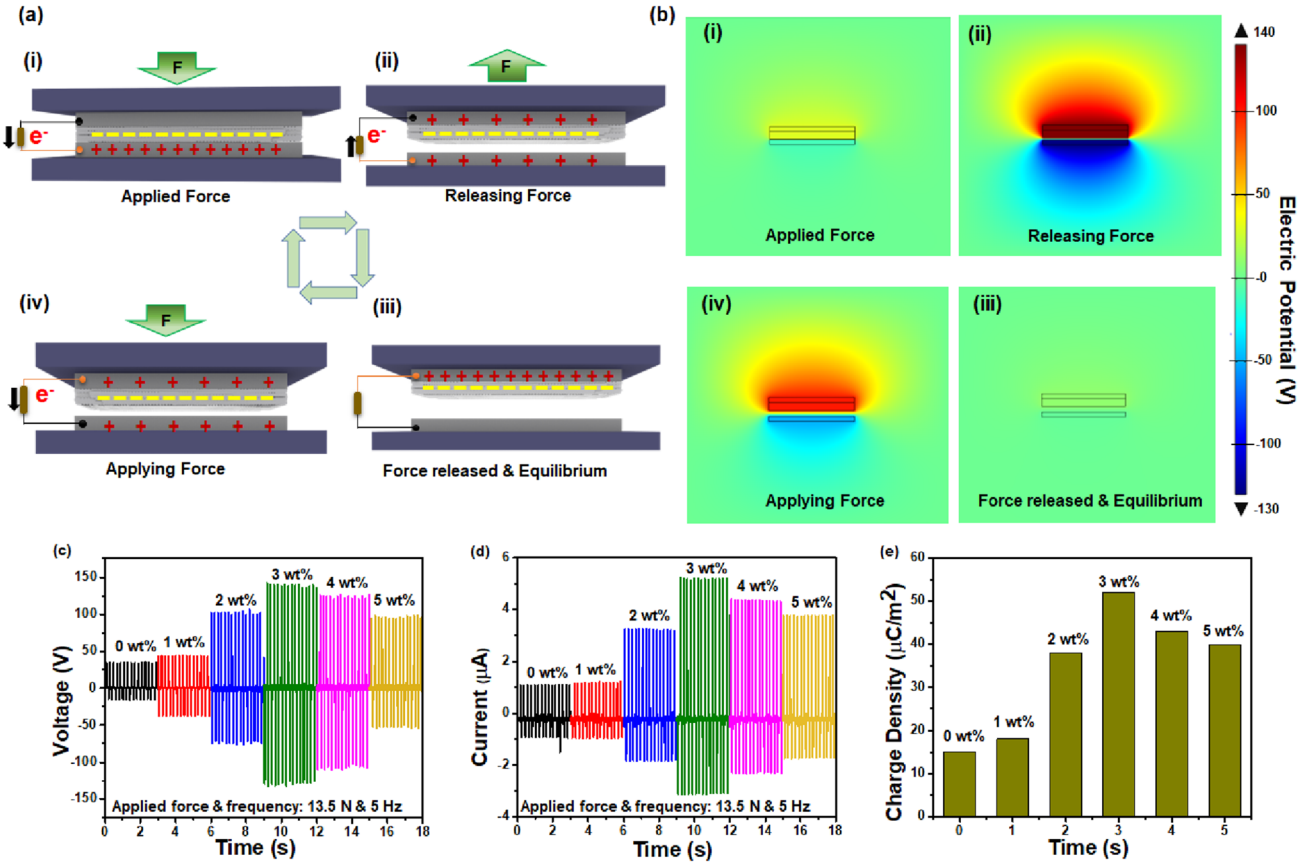

Fig. 3 **a** Working mechanism of the TENG and **b** COMSOL Multiphysics simulation results of the $ZnSnO_3$/PVDF-HFP-based TENG. **c–e** Electrical output performance of the TENGs based on the PVDF-HFP fibrous films with various $ZnSnO_3$ NPs concentrations

and surface charge density of the PVDF-HFP nanofibers while adding $ZnSnO_3$ NPs. Besides, when the filler concentration was increased more than 3 wt%, the output electrical performance of the TENG gradually decreased, i.e., to ~ 98 V, ~ 3.8 μA, and ~ 40 μC/m^2, respectively. This might be attributed to the reduced dielectric properties as mentioned before. The 3 wt% $ZnSnO_3$/PVDF-HFP fibrous film-based TENG exhibited the highest output electrical performance, which is considered as an optimal TENG device.

The electrical output performance of the proposed $ZnSnO_3$/PVDF-HFP fibrous film-based TENG was compared with various TENGs consisting of commercially available negative triboelectric films. Various negative triboelectric materials like polytetrafluoroethylene (PTFE), Kapton, polyethylene terephthalate (PET), fluorinated ethylene propylene (FEP), etc. were procured and utilized to fabricate various TENG devices with the same structure and dimension as that of the $ZnSnO_3$/PVDF-HFP fibrous film-based TENG. The electrical output from all the fabricated TENGs was investigated at constant mechanical force as shown in Fig. 4a and Fig. S7a–d of the SI. The generated electrical output from the optimized $ZnSnO_3$/PVDF-HFP fibrous film-based TENG was relatively high as compared to that of the commercially available triboelectric film-based TENGs. Fig. S8a and b of the SI shows the peak output voltage and current values of the optimized TENGs measured for various external load resistances from 100 Ω to 1 GΩ. The output voltage of the TENG increased with the increase of load resistance, and the output current decreased with increasing the resistance. Using the measured current at different load resistances, the corresponding power density was calculated. The following equation was used to calculate the effective power density (W_{eff}) of the PVDF-HFP and $ZnSnO_3$/PVDF-HFP fibrous film-based TENGs [40–42].

$$W_{eff} = \frac{I^2 R_L}{A} \tag{2}$$

Here, R_L denotes the external load resistance, I represents the peak output current of the TENG at the corresponding R_L, and A is an active area of the device (i.e., 4 cm^2). Figure 4b depicts the optimized output power density of the PVDF-HFP TENG as W_{eff} = ~ 0.1352 W/m^2 at 800 MΩ and $ZnSnO_3$/PVDF-HFP TENG as W_{eff} = ~ 1.6

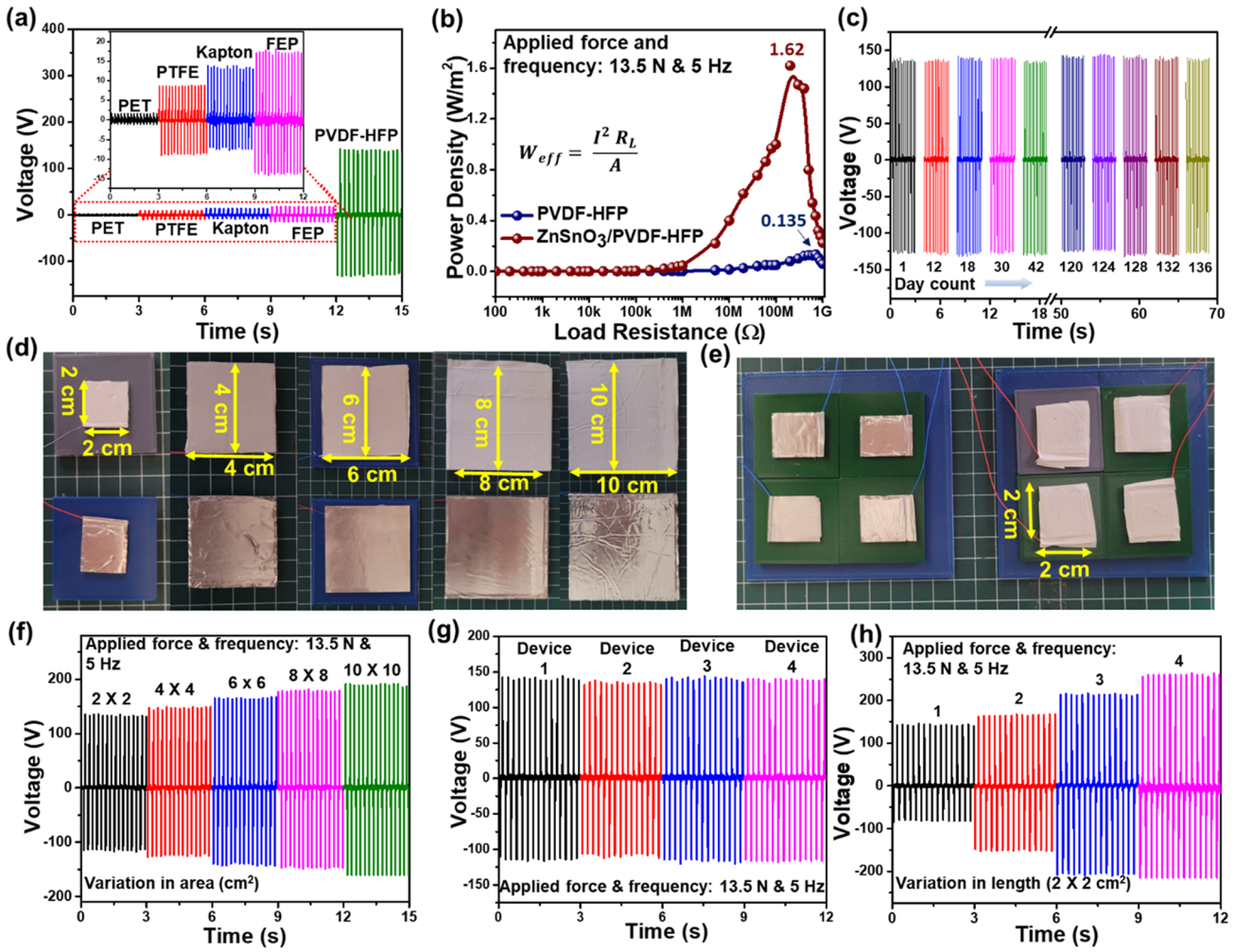

Fig. 4 **a** Electrical output voltage comparison for the PET, PTFE, Kapton, FEP, and $ZnSnO_3$/PVDF-HFP fibrous film-based TENGs. **b** Output power density curve of the PVDF-HFP and $ZnSnO_3$/PVDF-HFP fibrous film-based TENGs by varying the external load resistance from 100 Ω to 1 GΩ. **c** Stability in the electrical output produced by the TENG over more than three months. **d** Photographic images of the TENGs with different sizes. **e** Photographic image of four identical TENGs (2 × 2 cm^2). Voltage curves of **f** the TENGs with different active areas, **g** four similar TENGs, and **h** the TENGs with the increased number of devices

W/m^2 at 200 MΩ. The optimized 3 wt% $ZnSnO_3$/PVDF-HFP-based TENG exhibited the highest electrical output. Additionally, the long-term stability and sustainability measurements of the TENG were further studied as shown in Fig. 4c. The electrical output performance of the TENG was studied for a long duration of 70 days and the measurements were taken periodically. The voltage was measured every 6th day. The obtained output voltage remained almost the same (~ 138 V) of the TENG over 42 days. Thereafter, a similar stability measurement was done every 4th day from the 120th day of the TENG fabrication and it was observed that the output voltage still remained stable even on the 138th day as shown in Fig. 4c. Furthermore, the electrical output from the TENG was analyzed to find the size of the triboelectric film utilized on its electrical output performance. Initially, various optimized $ZnSnO_3$/PVDF-HFP fibrous films were fabricated in a square shape with side lengths of 2, 4, 6, 8, and 10 cm. All the films were utilized for the fabrication of different TENGs and operated with constant vertical mechanical force (13.5 N/5 Hz). The photographic image of the $ZnSnO_3$/PVDF-HFP fibrous film-based TENGs with different sizes is shown in Fig. 4d. To confirm the reproducibility of the $ZnSnO_3$/PVDF fibrous film-based TENG, four similar TENGs with an active area of 2 × 2 cm^2 were fabricated and their photographic image is shown in Fig. 4e. The produced electrical output from all the TENG with the increased length of the triboelectric active film in a square was analyzed. The electrical performance from the TENG with increasing the active triboelectric area is shown in Fig. 4f and Fig. S9a and b of the SI. It was observed that the electrical output from the TENG increased with an increased surface

area of the triboelectric active film. Furthermore, the electrical output produced by four similar TENGs (Fig. 4e) was analyzed at constant applied vertical mechanical force, as shown in Fig. 4g and Fig. S10a and b of the SI. The electrical output from all four TENGs was almost the same, indicating the reproducibility of the proposed TENG device. Thereafter, the electrical output was observed by connecting all the TENGs one by one in parallel connection as shown in Fig. 4h and Fig. S11a and b of the SI. The electrical output from all four TENGs (combined active area of 16 cm^2) connected parallelly generated an electrical output of ~ 250 V and ~ 21 µA. As previously observed, the TENG with a triboelectric active area of 16 cm^2 produced an electrical output of ~ 160 V and 5.5 µA, which is very less compared to the electrical output from the four TENGs connected parallelly. The enhancement in the electrical output from the TENGs connected in parallel connection is well-matched with the previously reported results [43–46].

The electrical output performance of the TENG under different conditions (such as force, frequency, and area) was also studied. Figure 5a–c shows the measured voltage, current, and charge density curves of the TENG under various applied forces. The electrical output was enhanced from ~ 55 V, ~ 1.8 µA, and ~ 30 µC/m^2 to ~ 195 V, ~ 7.4 µA, and ~ 76 µC/m^2 when the external force was increased from 4.5 to 27 N. However, the electrical output from the TENG got saturated with the applied forces more than 27 N as shown in Fig. 5a–c. The enhanced electrical output from the TENG is mainly due to the increased surface area of the utilized triboelectric film [47, 48]. However, the complete utilization of the available surface area in the triboelectric film results in saturated electrical output from the TENG irrespective of the increment in an applied force [46, 49, 50]. Figure 5d–f shows the electrical performance of the TENG

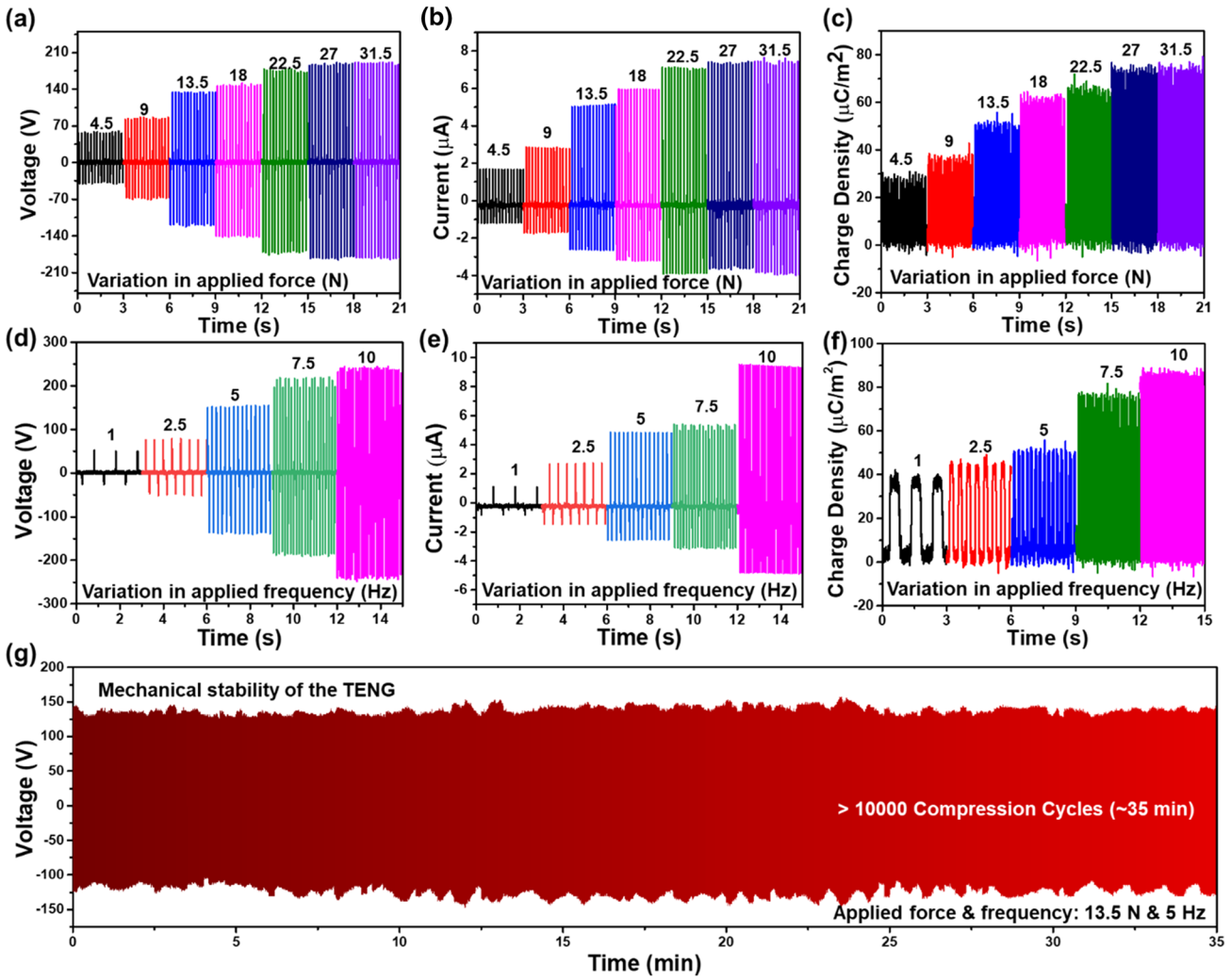

Fig. 5 Measured output voltage, current, and charge density curves of the TENG under various **a–c** applied forces and **d–f** applied frequencies. **g** Long-term mechanical stability test of the output voltage of the TENG

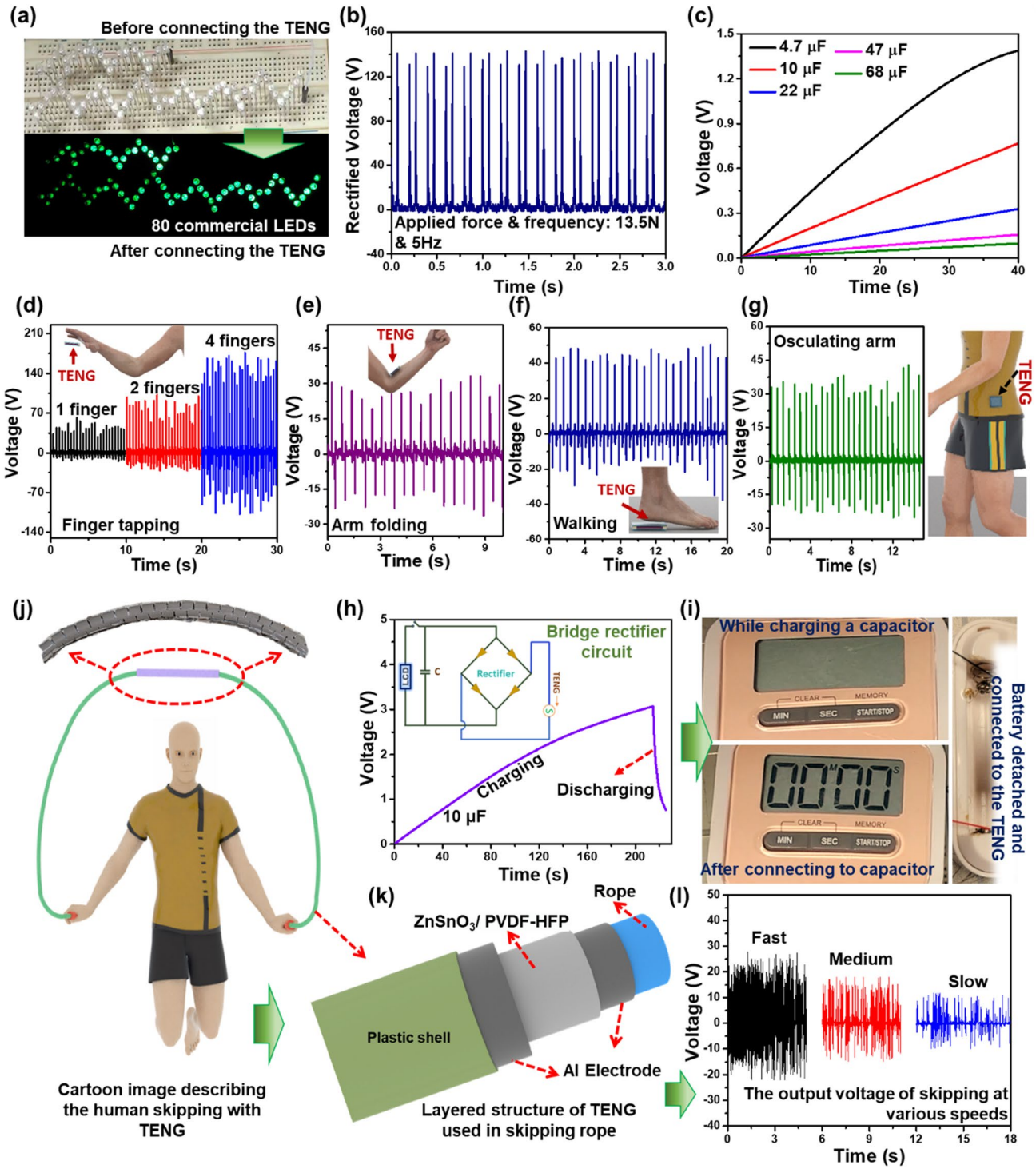

Fig. 6 Mechanical energy harvesting in real-time and commercial applications of the $ZnSnO_3$/PVDF-HFP fibrous film-based TENG. **a** Photographic images of the 80 commercially available green LEDs before and after powering using the TENG. **b** Measured rectified output voltage of the TENG. **c** Charging curves of various commercially available capacitors (i.e., 4.7, 10, 22, 47, and 68 μF) by the TENG. **d–g** Voltages obtained from the TENG device while finger tapping, arm folding, walking, and osculating arm, respectively. **h** Charging and discharging curve of the 10 μF capacitor connected to the full wave bridge rectifier circuit by the rectified output voltage from the TENG. **i** Photographic images of the LCD timer powered by the TENG using a bridge rectifier and a capacitor of 10 μF. **j** Schematic representation of the human body while skipping using TENG connected to the skipping rope. **k** Individual components of the TENG connected to the skipping rope. **l** Obtained electrical output of the TENG while skipping

when operated under different frequencies while the applied force was maintained constant. Figure 5g shows the measured output voltage of the TENG, which was continuously measured for more than 10,000 compression cycles. This confirms that the output performance of the TENG is more stable even after a long-term compression cycling test and there is no significant drop in the electrical output. Therefore, the generated highly stable electrical output of TENG is more beneficial for practical and commercial applications.

Figure 6 shows the practical and real-time applications of the proposed TENG. The obtained electrical output performance of the TENG was directly connected in a series to power various commercially available LEDs. Figure 6a and Video S1 of the SI show the photographic images of 80 green LEDs before and after glowing, powered by the TENG. Figure 6b shows the rectified electrical voltage using a bridge rectifier from the TENG, which was stored in a capacitor with a capacitance of 10 μF and used to power an LCD timer. This indicates that the bridge rectifier circuit successfully converts AC signals to direct current signals without any loss of the generated output voltage of the TENG. Figure 6c shows various commercially available capacitors with 4.7, 10, 22, 47, and 68 μF, charged by the TENG under the stable applied force and frequency of 13.5 N and 5 Hz, respectively. The TENG device can also be utilized to harvest various biomechanical energies involved in everyday human life, such as finger tapping, arm folding, walking, and osculating arm, as shown in Fig. 6d–g and Video S2 and Video S3 of the SI. Besides, Fig. 6h shows the charging and discharging curve of the commercial 10 μF capacitor charged by the TENG using a full wave bridge rectifier circuit to power the portable electronic gadgets. After charging the capacitor, the stored energy was directly used to power an LCD timer as shown in Fig. 6i and Video S1 of the SI. As observed previously, connecting multiple TENGs parallelly is more efficient than increasing the area (size) of the active triboelectric film for their fabrication. Therefore, multiple TENGs with similar dimensions were fabricated, connected parallelly, and integrated inside the skipping rope to harvest mechanical energy generated while skipping into electricity. Figure 6j–l and Video S4 of the SI show the harvesting of mechanical energy using the TENG from daily life human activities (skipping). Figure 6j shows the schematic diagram representing the human body while skipping and TENG connected to the skipping rope. Figure 6k shows the fabricated TENG and its individual components (such as plastic shell, Al electrodes, and $ZnSnO_3$/PVDF-HFP) connected to the skipping rope. Furthermore, the electrical output from the skipping rope TENG was investigated with variation in skipping speeds (slow, medium, and fast) as shown in Fig. 6l. An obvious increment in the electrical output from the skipping rope TENG was observed with increasing the skipping speed. The output voltage reached ~ 25 V from the skipping rope at high speeds. Therefore, the fabricated TENG is a promising device for powering low-power portable electronic gadgets and harvesting mechanical energy from daily human activities.

Conclusions

In summary, a high-performance TENG was successfully fabricated using $ZnSnO_3$/PVDF-HFP nanofibrous films. The $ZnSnO_3$ NPs were prepared by a simple hydrothermal method and further embedded into a PVDF-HFP polymer solution to form $ZnSnO_3$/PVDF-HFP fibrous film-based TENGs. The 3 wt% $ZnSnO_3$/PVDF-HFP fibrous film-based TENG exhibited the highest output performance, and the obtained output results of voltage, current, charge density, and power density were ~ 138 V, ~ 5 μA, and ~ 52 $\mu C/m^2$, and ~ 1.6 W/m^2, respectively. The highest electrical performance of the TENG was obtained mainly due to the effects of dielectric properties and enhanced surface charge density of the prepared nanofibrous films. Moreover, the robustness analysis of the TENG was investigated under various applied forces and frequencies, and the mechanical stability test was also performed under long-term compression cycles. Additionally, the generated electrical output from the TENG was able to instantaneously power various low-power portable electronic gadgets. Finally, the TENG was successfully demonstrated by generating electrical energy from mechanical energy harvesting while human skipping and another biomechanical harvesting. From all the above results, the proposed TENG integrated with $ZnSnO_3$/PVDF-HFP nanofibrous films can be employed for mechanical energy harvesting and powering various low-power portable electronics. The fabricated TENG that is easily scalable, highly efficient, and robust could be successfully implemented for harvesting various mechanical energies into electricity.

Supplementary Information The online version contains supplementary material available at https://doi.org/10.1007/s42765-023-00295-3.

Acknowledgements This work was supported by the National Research Foundation of Korea Grant funded by the Korean government (MSIP) (No. 2018R1A6A1A03025708).

Declarations

Conflict of interest The authors state that there are no conflicts of interest to disclose.

References

1. Turner JA. A Realizable Renewable Energy Future. *Science*. **1999**. https://doi.org/10.1126/science.285.5428.687.
2. Hu P, Yan L, Zhao C, Zhang Y, Niu J. Double-layer structured PVDF nanocomposite film designed for flexible nanogenerator exhibiting enhanced piezoelectric output and mechanical property. *Compos Sci Technol*. **2018**. https://doi.org/10.1016/j.compscitech.2018.10.021.
3. Chen C, Bai Z, Cao Y, Dong M, Jiang K, Zhou Y, Tao Y, Gu S, Xu J, Yin X, Xu W. Enhanced piezoelectric performance of $BiCl_3$/PVDF nanofibers-based nanogenerators. *Compos Sci Technol*. **2020**. https://doi.org/10.1016/j.compscitech.2020.108100.
4. Liu JX, Liu G, Guo ZH, Hu W, Zhang C, Pu X. Electret elastomer-based stretchable triboelectric nanogenerators with autonomously managed power supplies for self-charging systems. *Chem Eng J*. **2023**. https://doi.org/10.1016/j.cej.2023.142167.
5. Zi Y, Guo H, Wen Z, Yeh MH, Hu C, Wang ZL. Harvesting low-frequency (< 5 Hz) irregular mechanical energy: a possible killer application of triboelectric nanogenerator. *ACS Nano*. **2016**. https://doi.org/10.1021/acsnano.6b01569.
6. Yu J, Xian S, Zhang Z, Hou X, He J, Mu J, Geng W, Qiao X, Zhang L, Chou X. Synergistic piezoelectricity enhanced $BaTiO_3$/polyacrylonitrile elastomer-based highly sensitive pressure sensor for intelligent sensing and posture recognition applications. *Nano Res*. **2022**. https://doi.org/10.1007/s12274-022-5084-x. https://doi-org-ssl.openlink.khu.ac.kr/.
7. Wang J, Wu C, Dai Y, Zhao Z, Wang A, Zhang T, Wang ZL. Achieving ultrahigh triboelectric charge density for efficient energy harvesting. *Nat Commun*. **2017**. https://doi.org/10.1038/s41467-017-00131-4.
8. Li X, Luo J, Han K, Shi X, Ren Z, Xi Y, Ying Y, Ping J, Wang ZL. Stimulation of ambient energy generated electric field on crop plant growth. *Nat Food*. **2022**. https://doi.org/10.1038/s43016-021-00449-9.
9. Jiang C, Li X, Ying Y, Ping J. A multifunctional TENG yarn integrated into agrotextile for building intelligent agriculture. *Nano Energy*. **2020**. https://doi.org/10.1016/j.nanoen.2020.104863.
10. Arica TA, Isık T, Guner T, Horzum N, Demir MM. Advances in Electrospun Fiber-Based Flexible Nanogenerators for Wearable Applications. *Macromol Mater Eng*. **2021**. https://doi.org/10.1002/mame.202100143.
11. Li Y, Xiao S, Luo Y, Tian S, Tang J, Zhang X, Xiong J. Advances in electrospun nanofibers for triboelectric nanogenerators. *Nano Energy*. **2022**. https://doi.org/10.1016/j.nanoen.2022.107884.
12. Wu C, Jiang P, Li W, Guo H, Wang J, Chen J, Prausnitz MR, Wang ZL. Self-powered iontophoretic transdermal drug delivery system driven and regulated by biomechanical motions. *Adv Funct Mater*. **2020**. https://doi.org/10.1002/adfm.201907378.
13. Jiang C, Wu C, Li X, Yao Y, Lan L, Zhao F, Ye Z, Ying Y, Ping J. All-electrospun flexible triboelectric nanogenerator based on metallic MXene nanosheets. *Nano Energy*. **2019**. https://doi.org/10.1016/j.nanoen.2019.02.052.
14. Fan C, Zhang Y, Liao S, Zhao M, Lv P, Wei Q. Manufacturing technics for fabric/fiber-based triboelectric nanogenerators: from yarns to micro-nanofibers. *Nanomater*. **2022**. https://doi.org/10.3390/nano12152703.
15. Bai Z, Yao Z, Wu G, Liu K, Ye D, Tao Y, Xiao S, Chen D, Deng Z, Xu J, Zhou Y. PU/PVDF blend nanofiber film with enhanced mechanical and piezoelectric performance for development of stable nanogenerators. *Sens Actuator A*. **2023**. https://doi.org/10.1016/j.sna.2023.114407.
16. Ruiz-Rosas R, Bedia J, Lallave M, Loscertales IG, Barrero A, Rodríguez-Mirasol J, Cordero T. The production of submicron diameter carbon fibers by the electrospinning of lignin. *Carbon*. **2010**. https://doi.org/10.1016/j.carbon.2009.10.014.
17. Beachley V, Wen X. Effect of electrospinning parameters on the nanofiber diameter and length. *Mater Sci Eng C*. **2009**. https://doi.org/10.1016/j.msec.2008.10.037.
18. Jiang T, Wang J, Xie L, Bai C, Wang M, Wu Y, Zhang F, Zhao Y, Chen B, Wang Y. In situ fabrication of lead-free $Cs_3Cu_2I_5$ nanostructures embedded in poly (vinylidene fluoride) electrospun fibers for polarized emission. *ACS Appl Nano Mater*. **2022**. https://doi.org/10.1021/acsanm.1c03323.
19. Joseph J, Kumar M, Tripathy S, Kumar GDVS, Singh SG, Vaniari SRK. A highly flexible tactile, sensor with self-poled electrospun PVDF nanofiber. *IEEE Sens J*. **2018**. https://doi.org/10.1109/ICSENS.2018.8589807.
20. Shi L, Jin H, Dong S, Huang S, Kuang H, Xu H, Chen J, Xuan W, Zhang S, Li S, Wang X. High-performance triboelectric nanogenerator based on electrospun PVDF-graphene nanosheet composite nanofibers for energy harvesting. *Nano Energy*. **2021**. https://doi.org/10.1016/j.nanoen.2020.105599.
21. Ye BU, Kim BJ, Ryu J, Lee JY, Baik JM, Hong K. Electrospun ion gel nanofibers for flexible triboelectric nanogenerator: electrochemical effect on output power. *Nanoscale*. **2015**. https://doi.org/10.1039/C5NR02602D.
22. Fan FR, Tang W, Wang ZL. Flexible nanogenerators for energy harvesting and self-powered electronics. *Adv Mater*. **2016**. https://doi.org/10.1002/adma.201504299.
23. Inaguma Y, Sakurai D, Aimi A, Yoshida M, Katsumata T, Mori D, Yeon J, Halasyamani PS. Dielectric properties of a polar $ZnSnO_3$ with $LiNbO_3$-type structure. *J Solid State Chem*. **2012**. https://doi.org/10.1016/j.jssc.2012.07.036.
24. Paria S, Karan SK, Bera R, Das AK, Maitra A, Khatua BB. A facile approach to develop a highly stretchable PVC/$ZnSnO_3$ piezoelectric nanogenerator with high output power generation for powering portable electronic devices. *Ind Eng Chem Res*. **2016**. https://doi.org/10.1021/acs.iecr.6b02172.
25. Lando JB, Olf HG, Peterlin A. Nuclear magnetic resonance and x-ray determination of the structure of poly (vinylidene fluoride). *J Polym Sci Part A*. **1966**. https://doi.org/10.1002/pol.1966.150040420.
26. Son JY, Lee G, Jo MH, Kim H, Jang HM, Shin YH. Heteroepitaxial ferroelectric $ZnSnO_3$ thin film. *J Am Chem Soc*. **2009**. https://doi.org/10.1021/ja903133n.
27. Alam MM, Ghosh SK, Sultana A, Mandal D. Lead-free $ZnSnO_3$/MWCNTs-based self-poled flexible hybrid nanogenerator for piezoelectric power generation. *Nanotechnol*. **2015**. https://doi.org/10.1088/0957-4484/26/16/165403.
28. Zhao C, Cai L, Wang K, Li B, Yuan S, Zeng Z, Zhao L, Wu Y, He Y. Novel Bi_2WO_6/$ZnSnO_3$ heterojunction for ultrasonic vibration driven piezocatalytic degradation of RhB. *Environ Pollut*. **2022**. https://doi.org/10.1016/j.envpol.2022.120982.
29. Sanad MMS, Elsherif SS, Eraky MS, Abdel-Monem YK. Hetero-valent cations-doped zinc stannate nanoparticles for optoelectronic and dielectric applications. *Mater Chem Phys*. **2022**. https://doi.org/10.1016/j.matchemphys.2022.126700.
30. Gnanamoorthy G, Yadav VK, Latha D, Karthikeyan V, Narayanan V. Enhanced photocatalytic performance of $ZnSnO_3$/rGO nanocomposite. *Chem Phys Lett*. **2020**. https://doi.org/10.1016/j.cplett.2019.137050.
31. Gao Y, Li L, Zu W, Sun Y, Guan J, Cao Y, Yu H, Zhang W. Preparation of dual Z-scheme Bi_2MoO_6/$ZnSnO_3$/ZnO heterostructure photocatalyst for efficient visible light degradation of organic pollutants. *J Inorg Organomet Polym Mater*. **2022**. https://doi.org/10.1007/s10904-022-02242-y.
32. Bai S, Tong W, Tian Y, Fu H, Zhao Y, Shu X, Luo R, Li D, Chen A. Facile synthesis of Pd-doped $ZnSnO_3$ hierarchical

microspheres for enhancing sensing properties of formaldehyde. *J Mater Sci*. **2019**. https://doi.org/10.1007/s10853-017-1588-2.
33. Zheng J, Hou H, Fu H, Gao L, Liu H. Size-controlled synthesis of porous $ZnSnO_3$ nanocubes for improving formaldehyde gas sensitivity. *RSC Adv*. **2021**. https://doi.org/10.1039/D1RA01852C.
34. Sasmal A, Patra A, Devi PS, Sen S. Space charge induced augmented dielectric permittivity and improved energy harvesting ability of nano-Ag decorated $ZnSnO_3$ filled PVDF based flexible nanogenerator. *Compos Sci Technol*. **2021**. https://doi.org/10.1016/j.compscitech.2021.108916.
35. Zha JW, Sun F, Wang SJ, Wang D, Lin X, Chen G, Dang ZM. Improved mechanical and electrical properties in electrospun polyimide/multiwalled carbon nanotubes nanofibrous composites. *J Appl Phys*. **2014**. https://doi.org/10.1063/1.4897230.
36. Saikh MM, Hoque NA, Biswas P, Rahman W, Das N, Das S, Thakur P. Self-polarized ZrO_2/Poly (vinylidene fluoride-co-hexafluoropropylene) nanocomposite-based piezoelectric nanogenerator and single-electrode triboelectric nanogenerator for sustainable energy harvesting from human movements. *Phys Status Solidi A*. **2021**. https://doi.org/10.1063/1.4897230.
37. Sasmal A, Sen S, Devi PS. Frequency dependent energy storage and dielectric performance of Ba-Zr Co-doped $BiFeO_3$ loaded PVDF based mechanical energy harvesters: Effect of corona poling. *Soft Matter*. **2020**. https://doi.org/10.1039/D0SM01031F.
38. Cho Y, Park JB, Kim BS, Lee J, Hong WK, Park IK, Jang JE, Sohn JI, Cha S, Kim JM. Enhanced energy harvesting based on surface morphology engineering of P (VDF-TrFE) film. *Nano Energy*. **2015**. https://doi.org/10.1016/j.nanoen.2015.07.006.
39. Tayyab M, Wang J, Wang J, Maksutoglu M, Yu H, Sun G, Yildiz F, Eginligil M, Huang W. Enhanced output in polyvinylidene fluoride nanofibers based triboelectric nanogenerator by using printer ink as nano-fillers. *Nano Energy*. **2020**. https://doi.org/10.1016/j.nanoen.2020.105178.
40. Xia K, Zhu Z, Fu J, Li Y, Chi Y, Zhang H, Du C, Xu Z. A triboelectric nanogenerator based on waste tea leaves and packaging bags for powering electronic office supplies and behavior monitoring. *Nano Energy*. **2019**. https://doi.org/10.1016/j.nanoen.2019.03.050.
41. Pang Y, Chen S, Chu Y, Wang ZL, Cao C. Matryoshka-inspired hierarchically structured triboelectric nanogenerators for wave energy harvesting. *Nano Energy*. **2019**. https://doi.org/10.1016/j.nanoen.2019.104131.
42. Manchi P, Graham SA, Patnam H, Paranjape MV, Yu JS. rGO-$ZnSnO_3$ nanostructure-embedded triboelectric polymer-based hybridized nanogenerators. *Adv Mater Technol*. **2022**. https://doi.org/10.1002/admt.202101460.
43. Wang Q, Chen M, Li W, Li Z, Chen Y, Zhai Y. Size effect on the output of a miniaturized triboelectric nanogenerator based on superimposed electrode layers. *Nano energy*. **2017**. https://doi.org/10.1016/j.nanoen.2017.09.030.
44. Wu Y, Luo Y, Qu J, Daoud WA, Qi T. Sustainable and shape-adaptable liquid single-electrode triboelectric nanogenerator for biomechanical energy harvesting. *Nano Energy*. **2020**. https://doi.org/10.1016/j.nanoen.2020.105027.
45. Hou X, Zhang L, Su Y, Gao G, Liu Y, Na Z, Xu Q, Ding T, Xiao L, Li L, Chen T. A space crawling robotic bio-paw (SCRBP) enabled by triboelectric sensors for surface identification. *Nano Energy*. **2023**. https://doi.org/10.1016/j.nanoen.2022.108013.
46. He W, Van Ngoc H, Qian YT, Hwang JS, Yan YP, Choi H, Kang DJ. Synthesis of ultra-thin tellurium nanoflakes on textiles for high-performance flexible and wearable nanogenerators. *Appl Surf Sci*. **2017**. https://doi.org/10.1016/j.apsusc.2016.09.157.
47. Chou X, Zhu J, Qian S, Niu X, Qian J, Hou X, Mu J, Geng W, Cho J, He J, Xue C. All-in-one filler-elastomer-based high-performance stretchable piezoelectric nanogenerator for kinetic energy harvesting and self-powered motion monitoring. *Nano Energy*. **2018**. https://doi.org/10.1016/j.nanoen.2018.09.006.
48. Zhang H, Lu Y, Ghaffarinejad A, Basset P. Progressive contact-separate triboelectric nanogenerator based on conductive polyurethane foam regulated with a Bennet doubler conditioning circuit. *Nano energy*. **2018**. https://doi.org/10.1016/j.nanoen.2018.06.038.
49. Niu X, Jia W, Qian S, Zhu J, Zhang J, Hou X, Mu J, Geng W, Cho J, He J, Chou X. High-performance PZT-based stretchable piezoelectric nanogenerator. *ACS Sustain Chem Eng*. **2018**. https://doi.org/10.1016/j.nanoen.2018.09.006.
50. Yu J, Hou X, Cui M, Zhang S, He J, Geng W, Mu J, Chou X. Highly skin-conformal wearable tactile sensor based on piezoelectric-enhanced triboelectric nanogenerator. *Nano Energy*. **2019**. https://doi.org/10.1016/j.nanoen.2019.103923.

Venkata Siva Kavarthapu is currently pursuing his integrated (M.S. and Ph.D.) degree from the Department of Electronics and Information Convergence Engineering under the supervision of Prof. Jae Su Yu at Kyung Hee University, Republic of Korea. He received a Bachelor of Engineering (B.E.; 2021) from Sathyabama Institute of Science and Technology, Tamilnadu, India. His current research interests are focused on developing various nanofiber-based flexible triboelectric/hybrid nanogenerators for physical sensing and small-scale mechanical/biomechanical energy harvesting applications.

Sontyana Adonijah Graham is currently pursuing his Ph.D. in Electronic Engineering under the supervision of Prof. Jae Su Yu. at Kyung Hee University, Republic of Korea. He received his Master's degree in Nanoscience and Nanotechnology (2017) at the National Center for Nanoscience and Nanotechnology, University of Madras, India. His research interest includes various energy harvesting applications,

biocompatible and bioinspired electronics and functional nanomaterials for electronics and biomedical applications.

Punnarao Manchi is currently pursuing his master's and doctoral course (Ph. D.) degree from the Department of Electronics and Information Convergence Engineering under the supervision of Prof. Jae Su Yu at Kyung Hee University, Republic of Korea. He received a Bachelor of Technology (B.Tech.; 2014) from the Department of Electronics and communication engineering, Jawaharlal Nehru Technological University, Kakinada, India. His current research interests are focused on wearable and flexible piezoelectric, triboelectric, and hybrid nanogenerators.

Mandar Vasant Paranjape pursued his Master's (2017) and Bachelors's (2015) degrees in physics from Mumbai University, India. Currently, he is pursuing his Ph.D. degree under the supervision of Prof. Jae Su Yu at Kyung Hee University, in the Republic of Korea. His research of research interest includes the synthesis and development of nanostructured materials to harvest energy with an application-oriented, well-designed triboelectric/hybrid nanogenerator.

Jae Su Yu received his Ph.D. degree in optoelectronic engineering from the Department of Information and Communications, Gwangju Institute of Science and Technology, Republic of Korea, in 2002. Afterward, he joined in Center for Quantum Devices, Northwestern University, Evanston, IL, as a Postdoctoral Fellow (2002). Since 2006, he is a Tenured Professor in the Department of Electronic Engineering, Director of the Institute for Wearable Convergence Electronics, Kyung Hee University, Republic of Korea. He has authored or co-authored more than 570 SCI(E) indexed journal papers. His recent research interests include supercapacitors, nanogenerators, solar cells, optical sensors, nanophotonics, and phosphors.